Flow (2025), **5** E4
doi:10.1017/flo.2024.35

FLOW CAMBRIDGE UNIVERSITY PRESS

RESEARCH ARTICLE

Digital twin of a large-aspect-ratio Rayleigh–Bénard experiment: role of thermal boundary conditions, measurement errors and uncertainties

Philipp P. Vieweg[1,2,*], Theo Käufer[2], Christian Cierpka[2] and Jörg Schumacher[2,3]

[1]Department of Applied Mathematics and Theoretical Physics, Wilberforce Road, Cambridge CB3 0WA, UK
[2]Institute of Thermodynamics and Fluid Mechanics, Technische Universität Ilmenau, Postfach 100565, 98684 Ilmenau, Germany
[3]Tandon School of Engineering, New York University, New York, NY 11021, USA
*Corresponding author. E-mail: ppv24@cam.ac.uk

Received: 26 August 2024; **Revised:** 26 November 2024; **Accepted:** 28 November 2024

Keywords: Rayleigh–Bénard convection; numerical simulation; laboratory experiment; thermal boundary conditions

Abstract

Albeit laboratory experiments and numerical simulations have proven themselves successful in enhancing our understanding of long-living large-scale flow structures in horizontally extended Rayleigh–Bénard convection, some discrepancies with respect to their size and induced heat transfer remain. This study traces these discrepancies back to their origins. We start by generating a digital twin of one standard experimental set-up. This twin is subsequently simplified in steps to understand the effect of non-ideal thermal boundary conditions, and the experimental measurement procedure is mimicked using numerical data. Although this allows for explaining the increased observed size of the flow structures in the experiment relative to past numerical simulations, our data suggests that the vertical velocity magnitude has been underestimated in the experiments. A subsequent reassessment of the latter's original data reveals an incorrect calibration model. The reprocessed data show a relative increase in u_z of roughly 24 %, resolving the previously observed discrepancies. This digital twin of a laboratory experiment for thermal convection at Rayleigh numbers $Ra = \{2, 4, 7\} \times 10^5$, a Prandtl number $Pr = 7.1$ and an aspect ratio $\Gamma = 25$ highlights the role of different thermal boundary conditions as well as a reliable calibration and measurement procedure.

Impact Statement

The formation and dynamics of large-scale flow structures in horizontally extended turbulent Rayleigh–Bénard convection is essential for an understanding of its heat transfer. By creating a digital twin of a laboratory experiment, we investigate the influence of realistic thermal boundary conditions, which always deviate from ideal ones, and measurement deviations on the discrepancies between experimental and simulation results. The insights gained have broad implications for engineering and technological heat transfer applications. Understanding these effects can improve thermal management systems in industrial processes and electronic devices and provide critical guidance for future laboratory set-ups in fluid mechanics studies.

1. Introduction

The presence of convection as one of the basic means of heat transfer is of paramount importance for many natural systems – including habitable conditions on Earth – and engineering problems.

Understanding it allows, for instance, one to predict (space) weather (Atkinson & Wu Zhang 1996; Schwenn 2006; Pulkkinen 2007), to exploit the induced pressure gradients across Earth's atmosphere by wind turbines (Hau 2013; Vallis 2017) or even to power electrical devices where thermal management has been optimised to get rid of an active fan (Shabany 2010).

This broad applicability of general insights on naturally driven thermal convection has been attracting an uncountable number of researchers over the past century towards its paradigm, Rayleigh–Bénard convection. Whilst the key idea of the latter is to transfer heat through a horizontal layer of fluid of thickness H that is heated from below and cooled from above while being subjected to gravity, the particular set-up can differ significantly depending on the approach. Figure 1(a,f) depicts typical configurations present in laboratory experiments (Moller, Resagk & Cierpka 2020; Moller 2022) and numerical simulations (Vieweg, Scheel & Schumacher 2021*b*; Vieweg 2023), respectively. Undoubtedly, our progress is partly driven by both the symbiosis and antibiosis between these different approaches, exploiting either complex measurement techniques or expensive computing facilities to generate data.

Arrangements like these have allowed us to prove the existence of long-living large-scale flow structures (Käufer *et al.* 2023; Vieweg 2023, 2024) in horizontally extended domains despite being superposed to turbulence on significantly smaller time and length scales. Depending on the thermal boundary conditions applied at the heated bottom and cooled top plane, these roll-like flow structures (see figure 1*a*) exhibit different properties. In a nutshell, one observes either turbulent superstructures (Pandey, Scheel & Schumacher 2018; Vieweg *et al.* 2021*b*) with a characteristic horizontal extension of $\Lambda_{char} \sim O(H)$, or the gradual aggregation of convection cells towards a flat convection roll or supergranule (Vieweg *et al.* 2021*b*, 2022, 2024; Vieweg 2023, 2024) with $\Lambda_{char} \gg O(H)$ depending on whether the temperature field or its vertical gradient, respectively, is spatially homogeneous at the horizontal boundaries of the fluid. These two situations are physically linked to limits of the ratio of thermophysical properties between the fluid and its adjacent solid (Hurle, Jakeman & Pike 1967; Chapman, Childress & Proctor 1980; Chapman & Proctor 1980; Otero *et al.* 2002). One way to quantify this ratio is via the thermal diffusivity κ (Hurle *et al.* 1967) – the latter of which controls the (time-dependent) relaxation of thermal perturbations occurring at the solid–fluid interface – such that these different forcings correspond to $\kappa_{st,sb}/\kappa_{fl} \to \infty$ and $\kappa_{st,sb}/\kappa_{fl} \to 0$, respectively. Interestingly, the thermal boundary conditions seem to dominate any variation of the strength of the thermal driving (as quantified via the Rayleigh number Ra) or working fluid (as specified by the Prandtl number Pr) in three-dimensional analyses (Vieweg *et al.* 2021*b*; Vieweg 2023, 2024).

Of course, these limits can only be approximated by real materials and material selection is often further constrained by requirements of the measurement techniques such as optical transparency. Figure 1(a) shows such a compromise when analysing the large-scale heat transfer patterns (Moller *et al.* 2020; Moller 2022). On the one hand, the glass plate on top of the fluid layer of interest allows optical access, but it leads to $\kappa_{st}/\kappa_{fl} = 2.5$ and needs to be cooled using a pressure-driven flow. On the other hand, the aluminium bottom plate offers $\kappa_{sb}/\kappa_{fl} = 435$ and can be heated quite uniformly via meandering channels. Despite a small temperature difference of approximately $2K$ between both plates (Moller 2022; Moller *et al.* 2022), a convection flow emerges in the water that is visualised by suspended (temperature-sensitive) tracer particles in a horizontal slab at mid-height. A detailed description of the laboratory experiment can be found in Moller (2022). This asymmetry of thermal boundary conditions has so far not been accounted for in simulations, resulting in unresolved discrepancies when comparing experimental and numerical results. Most strikingly, experiments suggested an increased size of the turbulent superstructures and decreased induced heat transfer across the fluid layer compared with simulations (Pandey *et al.* 2018; Moller, Resagk & Cierpka 2021; Vieweg *et al.* 2021*a*, *b*; Moller *et al.* 2022; Schneide *et al.* 2022; Käufer *et al.* 2023). Unfortunately, precise attributions of those disagreements have not yet been possible due to a lack of simulations that resemble the experiment – especially with respect to its thermal boundary conditions, strength of thermal driving and horizontal extent of the domain; all of which affect those disagreements – sufficiently.

This study aims to resolve the disagreements between laboratory experiments and numerical simulations by creating a digital twin that mimics the former's geometrical and thermophysical properties

https://doi.org/10.1017/flo.2024.35 Published online by Cambridge University Press

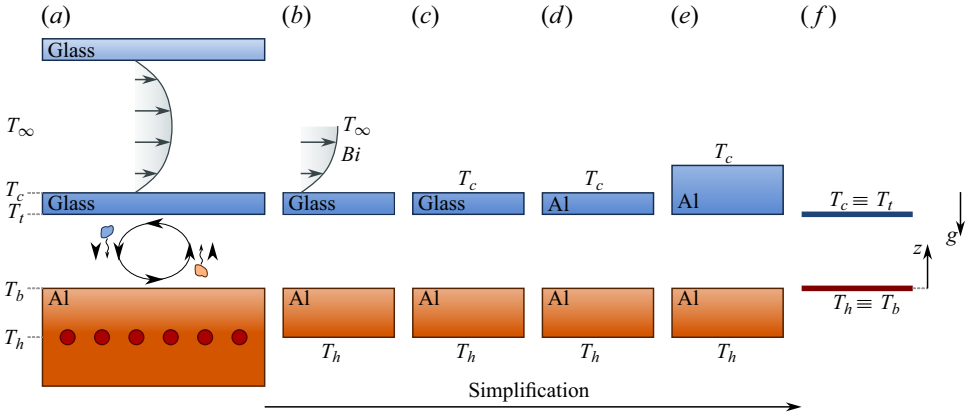

Figure 1. *Schematic configurations. We take the motivating laboratory experiment (EXP) on the left, create its digital twin that involves a Newton cooling (NC) condition and subsequently simplify the latter successively. Identifiers for different configurations are: (a) EXP, (b) NC, (c) CHTa, (d) CHTb, (e) CHTc, (f) DIR. The location of different temperatures is defined on the left, whereas panels (b–f) include the corresponding control parameters only; other values manifest dynamically. Here CHT stands for regular conjugate heat transfer and DIR for pure or classical Dirichlet boundary conditions.*

as well as boundary conditions. First, we study the impact of non-ideal and asymmetric thermal boundary conditions by an iterative simplification of this initial numerical configuration towards the classical numerical set-up (i.e. without solid plates). Although this exposes strong thermal variations at the upper solid–fluid interface for the digital twin and allows us to explain an increased size of flow structures, the observed heat transfer disagrees even stronger. Thus, and second, we successively modify the twin's true numerical data to imitate the experimentally present measurement procedure. This includes a systematic spatial averaging over interrogation windows, an erroneous detection of the mean solid–fluid interface temperatures and uncertainties for the particle image thermometry. Contrasting the modified numerical with experimental data at $Ra = \{2, 4, 7\} \times 10^5$, we find strong disagreements for the vertical or out-of-plane component of the velocity field. A subsequent reassessment of the original experimental data confirms that an incorrect calibration model led in the past to a systematic underestimation of this velocity component and, consequently, also to a reduced perceived heat transfer. Hence, this study highlights how digital twins of laboratory experiments can help in aligning the results of experimental and numerical approaches and understanding their discrepancies in detail.

2. Numerical method

2.1. Governing equations

Given the small mean temperature difference across the fluid layer in the motivating experimental configuration – see again figure 1(*a*) – we consider an incompressible flow based on the Oberbeck–Boussinesq approximation (Oberbeck 1879; Boussinesq 1903). This means that material parameters are assumed to be constant except for the mass density, the latter of which varies at first order (with respect to temperature) only when acting together with gravity (Rayleigh 1916; Vieweg 2023).

The three-dimensional equations of motion are solved by the spectral-element method Nek5000 (Fischer 1997; Scheel, Emran & Schumacher 2013). We non-dimensionalise the equations based on characteristic quantities of the fluid domain such as the fluid layer height H and temperatures at the bottom and top of this fluid layer, T_b and T_t, respectively. The characteristic (dimensional) temperature scale $\Delta T := \langle T_b - T_t \rangle_{A,t}$ is based on the mean temperatures across the corresponding horizontal cross-section A and time t. Together with the free-fall inertial balance, the free-fall velocity $U_f = \sqrt{\alpha g \Delta T H}$

https://doi.org/10.1017/flo.2024.35 Published online by Cambridge University Press

and time scale $\tau_f = H/U_f = \sqrt{H/\alpha g \Delta T}$ establish as further characteristic units. The pressure scale is $p_f = U_f^2 \rho_{ref,fl}$. Here, α is the volumetric thermal expansion coefficient of the fluid at constant pressure, g the acceleration due to gravity and $\rho_{ref,fl}$ the reference density of the fluid at reference temperature.

Despite this general approach, the governing equations differ depending on the phase of the domain. The equations relevant to the fluid domain translate into

$$\boldsymbol{\nabla} \cdot \boldsymbol{u} = 0, \tag{2.1}$$

$$\frac{\partial \boldsymbol{u}}{\partial t} + (\boldsymbol{u} \cdot \boldsymbol{\nabla})\boldsymbol{u} = -\boldsymbol{\nabla} p + \sqrt{\frac{Pr}{Ra}}\, \nabla^2 \boldsymbol{u} + T \boldsymbol{e}_z, \tag{2.2}$$

$$\frac{\partial T}{\partial t} + (\boldsymbol{u} \cdot \boldsymbol{\nabla}) T = \frac{1}{\sqrt{Ra\, Pr}}\, \nabla^2 T. \tag{2.3}$$

For the solid domains, we obtain a pure diffusion equation,

$$\frac{\partial T}{\partial t} = \frac{\kappa_\Phi}{\kappa_{fl}} \frac{1}{\sqrt{Ra\, Pr}}\, \nabla^2 T, \tag{2.4}$$

since the velocity is zero therein. In any of these equations, $\boldsymbol{u}$, T and p represent the (non-dimensional) velocity, temperature and pressure field, respectively.

The relative strength of the individual terms in the fluid-related equations (2.1)–(2.3) is specified by nothing but the Rayleigh and Prandtl number:

$$Ra = \frac{\alpha g \Delta T H^3}{\nu \kappa} \quad \text{and} \quad Pr = \frac{\nu}{\kappa}. \tag{2.5a,b}$$

The quantities ν and κ denote the kinematic viscosity and thermal diffusivity of the fluid, respectively. In contrast, the solid-related equation (2.4) requires the additional specification of the thermal diffusivity $\kappa_\Phi \equiv \lambda_{t,\Phi}/\rho_\Phi c_{p,\Phi}$ of a solid domain of interest $\Phi = \{\mathrm{st}, \mathrm{sb}\}$ relative to $\kappa_{fl} \equiv \lambda_{t,fl}/\rho_{ref,fl} c_{p,fl}$ from the fluid domain – hence, the ratio of thermal diffusivities κ_Φ/κ_{fl} turns up as an additional control parameter. Here, λ_t represents the thermal conductivity, ρ_Φ the mass density of the solid domain and c_p the specific heat capacity at constant pressure. This coefficient results simply from the above non-dimensionalisation based on parameters of the fluid domain together with the definitions in (2.5*a*,*b*). In this work we use the subscripts $\{\mathrm{fl}, \mathrm{st}, \mathrm{sb}\}$ to indicate the fluid, solid top or solid bottom domain, respectively.

2.2. Numerical domain and its boundary conditions

Resembling the laboratory experiment, the governing equations (2.1)–(2.4) are complemented by a closed three-dimensional domain with a square horizontal cross-section $A = \Gamma \times \Gamma$ and an aspect ratio $\Gamma := L/H$, where L is the horizontal length of the domain. The thickness of the solid top and bottom domains is defined via their respective aspect ratio $\Gamma_\Phi := H_\Phi/H$ and varies (just like their thermophysical properties) between the different configurations depicted in figure 1. The solid bottom domain is thus situated at $-\Gamma_{sb} \le z \le 0$, the fluid domain at $0 \le z \le 1$ and the solid top domain at $1 \le z \le 1 + \Gamma_{st}$.

The fluid obeys at any of its boundaries no-slip boundary conditions,

$$\boldsymbol{u} = 0 \quad \text{at all fluid boundaries.} \tag{2.6}$$

Moreover, we assume perfectly thermally insulated lateral boundaries such that

$$\frac{\partial T}{\partial x}(x = \pm\Gamma/2) = \frac{\partial T}{\partial y}(y = \pm\Gamma/2) = 0. \tag{2.7}$$

https://doi.org/10.1017/flo.2024.35 Published online by Cambridge University Press

The thermal boundary conditions at the different horizontal boundaries can conceptually be classified into (i) internal or passive and (ii) external or active ones. Concerning the former, the two (potential) solid–fluid interfaces require the continuity of both the temperature field and diffusive heat flux ($\boldsymbol{J}_{dif} = -\lambda_t \boldsymbol{\nabla} T$ in the dimensional framework), i.e.

$$T_{sb} = T_{fl} \quad \text{and} \quad \frac{\kappa_{sb}}{\kappa_{fl}} \frac{1}{\sqrt{Ra\,Pr}} \frac{\partial T_{sb}}{\partial z} = \frac{1}{\sqrt{Ra\,Pr}} \frac{\partial T_{fl}}{\partial z} \quad \text{at } z = 0, \tag{2.8a}$$

as well as

$$T_{st} = T_{fl} \quad \text{and} \quad \frac{\kappa_{st}}{\kappa_{fl}} \frac{1}{\sqrt{Ra\,Pr}} \frac{\partial T_{st}}{\partial z} = \frac{1}{\sqrt{Ra\,Pr}} \frac{\partial T_{fl}}{\partial z} \quad \text{at } z = 1. \tag{2.8b}$$

We term the corresponding temperature fields at these interfaces $T_b := T(z = 0)$ and $T_t := T(z = 1)$. The precise spatio-temporal temperature and heat flux distributions at these two boundaries manifest dynamically depending on the fluid flow, the latter of which is induced by the external thermal boundary conditions at $z = \{-\Gamma_{sb}, 1 + \Gamma_{st}\}$ in the first place. In the laboratory experiment, see again figure 1(*a*), these conditions differ significantly. We thus apply a classical Dirichlet as well as a Newton cooling boundary condition ($\lambda_t \boldsymbol{\nabla} T \cdot \boldsymbol{n} = h_{conv}(T - T_\infty)$ with the dimensional convection coefficient h_{conv} and wall-normal unity vector $\boldsymbol{n}$ in the dimensional framework) to its digital twin, such that

$$T(z = -\Gamma_{sb}) = T_h \tag{2.9a}$$

and

$$\frac{\kappa_{st}}{\kappa_{fl}} \frac{1}{\sqrt{Ra\,Pr}} \frac{\partial T}{\partial z} = Bi \frac{\kappa_{st}}{\kappa_{fl}} \frac{1}{\sqrt{Ra\,Pr}} (T - T_\infty) \quad \text{at } z = 1 + \Gamma_{st} \tag{2.9b}$$

at the bottom and top of the numerical domain, respectively. Note that the nature of these boundary conditions is quite different: while the former fixes the temperature itself at the boundary, the latter couples the local vertical heat flux to the temperature difference between the present temperature field and the undisturbed temperature T_∞ of the convectively cooling fluid. Hence, the Newton cooling boundary condition is less strict and allows for a non-uniform temperature distribution. Furthermore, it requires the additional quantification of the strength of convective cooling relative to thermal conduction at the corresponding boundary via the Biot number:

$$Bi = \frac{h_{conv} H}{\lambda_{t,st}}. \tag{2.10}$$

In the iterative process of simplifying the configuration, see again figure 1, we might eventually substitute this Newton cooling condition from (2.9*b*) by another Dirichlet condition:

$$T(z = 1 + \Gamma_{st}) = T_c. \tag{2.11}$$

At the end of this process, the solid domains will be omitted entirely and the internal thermal boundary conditions (2.8) will disappear – this is the case in most numerical Rayleigh–Bénard convection studies (Pandey *et al.* 2018; Krug, Lohse & Stevens 2020; Vieweg *et al.* 2021*b*) and depicted in figure 1(*f*).

Let us briefly summarise the different non-dimensional parameters that have been introduced. In a nutshell, we have collected (i) control parameters from the governing equations itself $\{Ra, Pr\}$, (ii) geometric parameters $\{\Gamma, \Gamma_{sb}, \Gamma_{st}\}$, (iii) thermophysical parameters $\{\kappa_{sb}/\kappa_{fl}, \kappa_{st}/\kappa_{fl}\}$, as well as (iv) thermal boundary condition parameters that are either $\{T_h, Bi, T_\infty\}$ or $\{T_h, T_c\}$ depending on the precise configuration. Thereby, we have also introduced the temperature fields $\{T_\infty, T_c, T_t, T_b, T_h\}$ at the coordinates shown in figure 1(*a*). Note that the internal temperatures at the solid–fluid interfaces are a function of space and time, whereas the external temperatures will be considered to be constant.

https://doi.org/10.1017/flo.2024.35 Published online by Cambridge University Press

2.3. Initial condition

The applied external temperatures can be used to compute a one-dimensional, stationary diffusive temperature profile across the different layers given their geometrical and thermophysical properties. Altered by some tiny random thermal noise $0 \leq \Upsilon \leq 10^{-3}$ and together with a fluid at rest (i.e. $\boldsymbol{u}(t=0)=0$), this profile is used as the initial condition for each simulation.

The stationary temperature profiles within the three layers at hand can generally be expressed via

$$T_{st}(z_{st}, t=0) = T_t - (T_t - T_c)\frac{z_{st}}{\Gamma_{st}} \quad \text{for } z_{st} \equiv z - 1 \in [0, \Gamma_{st}], \tag{2.12}$$

$$T_{fl}(z_{fl}, t=0) = T_b - (T_b - T_t) z_{fl} \quad \text{for } z_{fl} \equiv z \in [0, 1], \tag{2.13}$$

$$T_{sb}(z_{sb}, t=0) = T_h - (T_h - T_b)\frac{z_{sb}}{\Gamma_{sb}} \quad \text{for } z_{sb} \equiv z + \Gamma_{sb} \in [0, \Gamma_{sb}]. \tag{2.14}$$

Since the diffusive heat flux needs to match at the various interfaces, these profiles are coupled. In the case of a present Newton cooling (i.e. given $\{T_h, Bi, T_\infty\}$), the boundary conditions from (2.9) form together with (2.8) a linear system of equations and yield

$$T_c = \{[h_{st}(h_{fl} + h_{sb}) + h_{fl}h_{sb}]h_{Bi}T_\infty + h_{st}h_{fl}h_{sb}T_h\}/D, \tag{2.15a}$$

$$T_t = \{h_{st}(h_{fl} + h_{sb})h_{Bi}T_\infty + (h_{st} + h_{Bi})h_{fl}h_{sb}\ T_h\}/D, \tag{2.15b}$$

$$T_b = \{h_{st}h_{fl}h_{Bi}T_\infty + [h_{st}(h_{fl} + h_{Bi}) + h_{fl}h_{Bi}]h_{sb}T_h\}/D, \tag{2.15c}$$

with

$$D := h_{st}h_{fl}h_{sb} + [h_{st}(h_{fl} + h_{sb}) + h_{fl}h_{sb}]h_{Bi}, \quad h_{Bi} := Bi\frac{\kappa_{st}}{\kappa_{fl}}\frac{1}{\sqrt{Ra\,Pr}}, \tag{2.15d}$$

$$h_{st} := \frac{\kappa_{st}}{\kappa_{fl}}\frac{1}{\sqrt{Ra\,Pr}}\frac{1}{\Gamma_{st}}, \quad h_{fl} := \frac{Nu}{\sqrt{Ra\,Pr}}, \quad h_{sb} := \frac{\kappa_{sb}}{\kappa_{fl}}\frac{1}{\sqrt{Ra\,Pr}}\frac{1}{\Gamma_{sb}}, \tag{2.15e}$$

where the last line describes the various heat transfer coefficients h_Φ or thermal conductances $h_\Phi\Gamma^2$ in the solid and fluid domains. In the opposing case where the Newton condition (2.9*b*) is substituted by the second Dirichlet condition (2.11) (i.e. given $\{T_h, T_c\}$),

$$T_t = \frac{(h_{st} + h_{st}h_{sb}/h_{fl})T_c + h_{sb}T_h}{h_{st} + h_{sb} + h_{st}h_{sb}/h_{fl}}, \tag{2.16a}$$

$$T_b = T_t + \frac{h_{st}}{h_{fl}}(T_t - T_c), \tag{2.16b}$$

can be deduced.

Remember that we used the temperature drop across the fluid layer as a characteristic quantity of the system in § 2.1. However, as it might have become clear earlier from (2.8) or here from the above initial conditions in (2.15) and (2.16), the temperatures at these solid–fluid interfaces manifest dynamically. Considering the non-dimensionalisation of this mean temperature drop across the fluid layer, i.e. $\langle T_b - T_t\rangle_{A,t} \equiv \langle T(z=0) - T(z=H)\rangle_{A,t} = \Delta T\langle\tilde{T}(z=0) - \tilde{T}(z=1)\rangle_{\tilde{A},\tilde{t}} = \Delta T\widetilde{\Delta T}$ (Otero *et al.* 2002; Vieweg 2023) where tildes indicate non-dimensional quantities, this implies that one needs either to account for the non-dimensional temperature drop $\widetilde{\Delta T} \equiv \Delta T_N$ in various equations or to make sure that $\Delta T_N \simeq 1$ by adjusting the external temperatures correspondingly. We have decided to go with the latter option as this resembles the common situation in Rayleigh–Bénard convection.

Furthermore, note in particular that h_{fl} from (2.15*e*) represents the effective thermal heat transfer coefficient of the fluid layer as it comprises the Nusselt number $Nu \geq 1$ (see (3.2)). Considering that the initial condition represents a fluid at rest, one might set $Nu(t=0) = 1$. However, in this work we assume that $Nu(t=0) > 1$ to account for the thermal capacities of the different layers and aim at reaching

https://doi.org/10.1017/flo.2024.35 Published online by Cambridge University Press

statistically steady conditions thereby more quickly. Of course, the final statistically stationary value of Nu is not known *a priori*.

Hence, we run in this work various preliminary two- and three-dimensional simulations in advance of each production simulation in order to find the optimal $\{T_h, Bi, T_\infty\}$ or $\{T_h, T_c\}$ as well as the induced global heat transfer Nu, the latter of which is then used in the initial condition. This iterative procedure ensures that $\Delta T_N \simeq 1$ right from the initialisation.

3. The impact of non-ideal thermal boundary conditions

3.1. The digital twin

In order to study the effect of experimentally present thermal boundary conditions, we start by creating a digital twin of the motivating laboratory experiment. The experiment configuration – see again figure 1(*a*) – suggests to apply the Dirichlet and Newton cooling boundary conditions from (2.9) at the bottom and top, respectively. The aspect ratio of the closed domain $\Gamma = 25$, the thickness of the aluminium bottom plate $\Gamma_{sb} = 0.66$ with a relative thermal diffusivity $\kappa_{sb}/\kappa_{fl} = 435$, and $\Gamma_{st} = 0.29$ with $\kappa_{st}/\kappa_{fl} = 2.5$ for the glass top plate. The resulting twin is sketched in figure 1(*b*). Furthermore, we consider $Ra = 2 \times 10^5$ and $Pr = 7.1$ just like in the experiment (Moller 2022; Moller *et al.* 2022).

Note that while thermal conduction through or in the lateral walls can become significant especially for slender convection cells (Stevens, Lohse & Verzicco 2014), we assume them to be adiabatic in our motivating experimental set-up (and thus also the digital twin; see (2.7)) due to several reasons. First, the experiment offers a large aspect ratio $\Gamma \gg 1$ and so the total area of the side walls is by an order of magnitude smaller than that of the top and bottom plates. Second, the mean temperature in the turbulent flow is held at room temperature during experiments and the side walls are additionally insulated. Third, both the fluid's heat transfer coefficient and horizontal cross-section are significantly larger than those of the side walls, rendering vertical heat transfer within the latter negligible.

The experimentally present convection coefficient h_{conv} – entering the non-dimensional control parameter Bi – cannot be extracted from the collected experimental data. We thus estimate its value based on two different approaches. On the one hand, we consider a one-dimensional flow over a heated flat plate of uniform temperature with its evolving laminar boundary layer. On the other hand, we consider the Sieder–Tate law for fully transitioned laminar pipe flows based on the corresponding hydraulic diameter (Incropera & DeWitt 1996). These two approaches yield $Bi \simeq 5.1$ and $Bi \simeq 6.0$, respectively, and we consider both of these values in the following.

3.2. Simplification of the numerical domain

From the perspective of the convective fluid layer, the thermal boundary condition is determined by both the thermophysical and geometric properties of a solid plate adjacent to it. Firstly, if the ratio of thermal diffusivities $\kappa_\Phi/\kappa_{fl} \to \infty$, thermal perturbations relax much quicker in the solid plate compared with the fluid and so the former is a perfect thermal conductor which can be considered isothermal. *Vice versa*, the plate appears as a thermal insulator and the provided (constant) heat flux is independent of the fluid motion in the opposite case of $\kappa_\Phi/\kappa_{fl} \to 0$ (Hurle *et al.* 1967). Note further that the Nusselt number affects the effectively present ratio via $\kappa_{fl,eff} = Nu\,\kappa_{fl}$. Secondly, also the geometry plays a crucial role. Consider therefore the horizontal and vertical thermal diffusion time scales $\tau_{\kappa,\Phi,h} := L_\Phi^2/\kappa_\Phi$ and $\tau_{\kappa,\Phi,v} := (\Gamma_\Phi H)^2/\kappa_\Phi$, respectively, inside an infinitely thin solid plate. In this case of $\Gamma_\Phi \to 0$, the external thermal boundary condition affects immediately also the solid–fluid interface since $\tau_{\kappa,\Phi,v} \ll \tau_{\kappa,\Phi,h}$. In other words, the external thermal boundary condition cannot be relaxed by thermal diffusion inside the solid plate and, thus, leaves a significant footprint on the solid–fluid interface. This footprint vanishes only in the opposite limit $\tau_{\kappa,\Phi,v} \gg \tau_{\kappa,\Phi,h}$, i.e. for $\Gamma_\Phi H \gg L_\Phi$.

For these reasons, we study the effect of varying thermal boundary conditions by considering different configurations of the numerical domain – in terms of both the thermophysical and geometric

https://doi.org/10.1017/flo.2024.35 Published online by Cambridge University Press

Table 1. *Simulation parameters. The Prandtl number $Pr = 7.1$ and aspect ratio $\Gamma = 25$ with all walls of the closed domain obeying no-slip boundary conditions and lateral boundaries being perfectly insulated. The table contains beside the run identifier, the Rayleigh number Ra, the total number of spectral elements $N_e = N_{e,x} \times N_{e,y} \times (N_{e,z,sb} + N_{e,z,fl} + N_{e,z,st})$ (with the polynomial order $N = 8$ on each spectral element, except for run 4NC6 where $N = 6$), the Biot number Bi, as well as applied and resulting (spatio-temporally mean) temperatures at the different horizontal interfaces $\{T_\infty, T_c, T_t, T_b, T_h\}$. Dynamically resulting temperatures are indicated by a quantification of the (temporal) standard deviation. The spatio-temporal average of T_t and T_b is typically $O(10^{-4})$ and $O(10^{-5})$ off its ideal value of 0 and 1, respectively. The run time of all simulations $t_r = 12\,000$ while the last $10\,000$ have been used to gather results and statistical values. Motivating laboratory experiments are contrasted via rows with a grey text colour while their printed temperatures assume ideal identifications of interface temperatures. The identifiers refer to the different numerical configurations introduced in figure 1.*

Run	*Ra*	N_e	*Bi*	T_∞	T_c	T_t	T_b	T_h
2EXP	2×10^5			−0.880		$\pm O(10^{-2})$	$1 \pm O(10^{-2})$	1.2508
2NC5	2×10^5	$85^2 \times$ (3+4+2)	5.1	−1.015	$-0.605 \pm O(10^{-4})$	$\pm O(10^{-4})$	$1 \pm O(10^{-5})$	1.0079
2NC6	2×10^5	$85^2 \times$ (3+4+2)	6.0	−0.955	$-0.608 \pm O(10^{-4})$	$\pm O(10^{-4})$	$1 \pm O(10^{-5})$	1.0079
2CHTa	2×10^5	$85^2 \times$ (3+4+2)			−0.603	$\pm O(10^{-4})$	$1 \pm O(10^{-5})$	1.0079
2CHTb	2×10^5	$85^2 \times$ (3+4+2)			−0.0035	$\pm O(10^{-5})$	$1 \pm O(10^{-5})$	1.0079
2CHTc	2×10^5	$85^2 \times$ (3+4+2)			−0.0079	$\pm O(10^{-5})$	$1 \pm O(10^{-5})$	1.0079
2DIR	2×10^5	$85^2 \times$ (3+4+2)				0	1	
4EXP	4×10^5			−1.356		$\pm O(10^{-2})$	$1 \pm O(10^{-3})$	1.2218
4NC6	4×10^5	$125^2 \times$ (6+6+3)	6.0	−1.175	$-0.746 \pm O(10^{-4})$	$\pm O(10^{-4})$	$1 \pm O(10^{-5})$	1.0098
7EXP	7×10^5			−1.626		$\pm O(10^{-2})$	$1 \pm O(10^{-3})$	1.2232
7NC6	7×10^5	$125^2 \times$ (6+6+3)	6.0	−1.395	$-0.886 \pm O(10^{-4})$	$\pm O(10^{-4})$	$1 \pm O(10^{-5})$	1.0116

properties – as presented in figure 1. Commencing with the digital twin, we successively simplify the configuration. First, we replace the Newton cooling boundary condition (2.9*b*) by another (stronger) Dirichlet condition (2.11) (see panel *c*) similar to typical conjugate heat transfer problems (Perelman 1961; Foroozani, Krasnov & Schumacher 2021). Second, we replace the glass top plate by an aluminium one such that $\kappa_{st}/\kappa_{fl} = \kappa_{sb}/\kappa_{fl}$ (see panel *d*). Third, the thickness of the top plate is adjusted to that of the bottom plate such that $\Gamma_{st} = \Gamma_{sb}$ (see panel *e*). Fourth and finally, we omit the solid top and bottom aluminium plates entirely and apply Dirichlet conditions directly to the fluid layer (see panel *f*) – this situation corresponds to $\{\Gamma_{st}, \Gamma_{sb}\} \to 0$ and converged to or represents the traditional Rayleigh–Bénard convection configuration. Note that the different successive modifications build up on each other.

3.3. Comparison of different configurations of the numerical domain

Table 1 summarises the final control parameters of each (production) simulation together with the spatial resolutions across the different parts of the domain. As some of the interface temperatures manifest dynamically, we include for those ones also the temporal standard deviation (around the spatio-temporal

https://doi.org/10.1017/flo.2024.35 Published online by Cambridge University Press

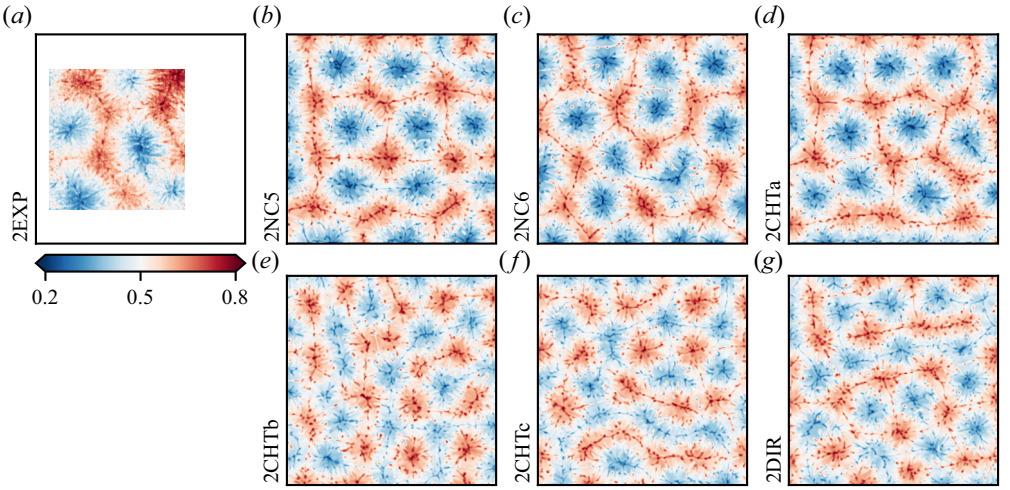

Figure 2. *Flow structures at different thermal boundary conditions. We visualise the instantaneous temperature field $T(x, y, z = 0.5, t = t_r)$ of (a) the laboratory experiment and (b–g) each simulation at $Ra = 2 \times 10^5$. The flow structures depend clearly on the thermal boundary conditions; see also figure 1. The colour bar applies to all panels.*

mean temperatures). After initialising the flows with these parameters, the long-living large-scale flow structures form and develop a statistically stationary pattern size within the first $2000\tau_f$. This implies that also other global measures such as the heat and momentum transfer have converged (Vieweg *et al.* 2021*b*, 2022; Vieweg 2023). We omit this transient period from our evaluation and run each simulation for additional $10\,000\tau_f$ that will be analysed. Note that this runtime of the simulations exceeds the runtime of the laboratory experiments (Moller 2022; Moller *et al.* 2022).

Figure 2 compares the different resulting flows by means of their final instantaneous temperature fields at mid-plane – thermal boundary conditions clearly affect pattern formation. Structures become smaller for (stricter) conditions that are more similar to the plate-less Dirichlet configuration shown in panel (*g*), being in line with our previous studies (Vieweg *et al.* 2021*b*, 2022; Vieweg 2023). *Vice versa*, when this ideal configuration is successively left and the horizontal extent of the domain becomes smaller relative to the growing flow structures, the effect of the lateral side walls becomes stronger and they seem to impose preferential directions. This is most prominent in panels (*b–d*) where the solid top plate is made of glass and so $\kappa_{st}/\kappa_{fl} \sim O(10^0)$. Note that it was not possible to measure near the side walls in the motivating laboratory experiment (Moller 2022), leading to the restricted field of view in panel (*a*). A comparison of this experimentally observed flow with the entire set of simulations confirms that the digital twins resemble the experiment best, particularly at $Bi = 6.0$.

Extending this first visual or qualitative impression, we proceed by quantifying various measures of the flows. Foremost, we consider the largest instantaneous horizontal temperature difference

$$\max(\Delta_{hor} T_t)\ (t) = \max_{x,y}(T_t) - \min_{x,y}(T_t) \tag{3.1}$$

at the (proner) upper solid–fluid interface. Secondly, this is complemented by the instantaneous standard deviation $\mathrm{std}(T_t)$. These two quantities are used to probe the inhomogeneity of the temperature field at this interface. Thirdly, we quantify the ratio of the (average) total heat current $\boldsymbol{J} = \boldsymbol{u}T + \boldsymbol{J}_{dif}$ across the fluid layer to the diffusive heat current $\boldsymbol{J}_{dif} = -\boldsymbol{\nabla} T/\sqrt{Ra\,Pr}$ that took place in the case of pure heat

https://doi.org/10.1017/flo.2024.35 Published online by Cambridge University Press

Table 2. *Global characteristic measures of the simulations from table 1. This table contains the maximum instantaneous temperature difference at the upper solid–fluid interface* $\max(\Delta_{hor}T_t)$*, the instantaneous standard deviation of the temperature field at this interface* $std(T_t)$*, the true global Nusselt number Nu (which includes the diffusive heat transport), the experimentally accessible Nusselt number* Nu_{exp}*, the Reynolds number Re, as well as the integral length scale of the temperature field* Λ_T*. All values are provided as temporal means together with the corresponding standard deviation. Motivating laboratory experiments are contrasted via rows with a grey text colour and are based on a restricted field. Revised values of their* Nu_{exp} *and Re are reported in § 4.4.*

Run	$\max(\Delta_{hor}T_t)$	$\mathrm{std}(T_t)$	Nu	Nu_{exp}	Re	Λ_T
2EXP				4.11 ± 0.22	12.48 ± 0.24	7.53 ± 0.22
2NC5	0.598 ± 0.016	$0.084 \pm O(10^{-4})$	5.23 ± 0.03	5.27 ± 0.05	15.78 ± 0.05	8.07 ± 0.25
2NC6	0.586 ± 0.017	$0.083 \pm O(10^{-4})$	5.24 ± 0.03	5.33 ± 0.05	15.82 ± 0.05	7.90 ± 0.26
2CHTa	0.531 ± 0.018	$0.073 \pm O(10^{-4})$	5.22 ± 0.03	5.26 ± 0.05	15.75 ± 0.06	7.59 ± 0.21
2CHTb	0.007 ± 0.000	$0.001 \pm O(10^{-5})$	5.15 ± 0.03	5.19 ± 0.05	15.65 ± 0.05	6.56 ± 0.19
2CHTc	0.010 ± 0.000	$0.002 \pm O(10^{-5})$	5.15 ± 0.03	5.20 ± 0.05	15.66 ± 0.05	6.62 ± 0.19
2DIR	0	0	5.15 ± 0.03	5.19 ± 0.05	15.66 ± 0.06	6.60 ± 0.19
4EXP				5.69 ± 0.27	19.20 ± 0.19	7.69 ± 0.27
4NC6	0.561 ± 0.017	$0.076 \pm O(10^{-4})$	6.44 ± 0.03	6.49 ± 0.07	23.32 ± 0.08	8.04 ± 0.30
7EXP				5.86 ± 0.24	26.13 ± 0.27	7.77 ± 0.53
7NC6	0.541 ± 0.018	$0.073 \pm O(10^{-4})$	7.64 ± 0.04	7.68 ± 0.09	31.84 ± 0.11	8.43 ± 0.39

conduction by the (global) Nusselt number (Otero *et al.* 2002; Vieweg 2023)

$$Nu(t) = \frac{\langle \boldsymbol{J} \cdot \boldsymbol{e}_z \rangle_V}{\langle \boldsymbol{J}_{dif} \cdot \boldsymbol{e}_z \rangle_V} = \left\langle -\frac{\partial T}{\partial z} + \sqrt{Ra\,Pr}\, u_z T \right\rangle_V = 1 + \sqrt{Ra\,Pr}\, \langle u_z T \rangle_V . \tag{3.2}$$

Fourthly, we assess the momentum transport using the Reynolds number (Scheel & Schumacher 2017)

$$Re(t) := \sqrt{\frac{Ra}{Pr}} u_{rms} \quad \text{with } u_{rms} := \sqrt{\langle \boldsymbol{u}^2 \rangle_V}. \tag{3.3}$$

Finally, the so-called integral length scale (Parodi *et al.* 2004)

$$\Lambda_T(z = 0.5, t) := 2\pi \frac{\int_{k_h} [E_{TT}/k_h]\, \mathrm{d}k_h}{\int_{k_h} E_{TT}\, \mathrm{d}k_h} \tag{3.4}$$

is used to measure the present characteristic pattern size. Here $E_{TT} \equiv E_{TT}(k_h, z = 0.5, t)$ represents the azimuthally averaged Fourier energy spectrum of the temperature field and k_h the horizontal wavenumber (Vieweg 2023). All of these quantities are summarised and contrasted with respect to their temporal mean value and standard deviation in table 2.

Our quantification of thermal inhomogeneities highlights prominently that the upper solid–fluid interface can become strongly inhomogeneous depending on the choice of the plate material. Given a glass plate with $\kappa_{st}/\kappa_{fl} \sim O(10^0)$, the horizontal temperature difference can reach 60 % of the temperature drop across the Rayleigh–Bénard convection layer. In contrast, this is reduced to 1 % once the plate is made of aluminium with $\kappa_{st}/\kappa_{fl} \sim O(10^2)$. This observation is qualitatively confirmed by the corresponding standard deviation of the interface temperature and can directly be related to the different ratios of thermal diffusion time scales $\tau_{\kappa,fl}/\tau_{\kappa,st} \equiv \kappa_{st}/\kappa_{fl}$.

https://doi.org/10.1017/flo.2024.35 Published online by Cambridge University Press

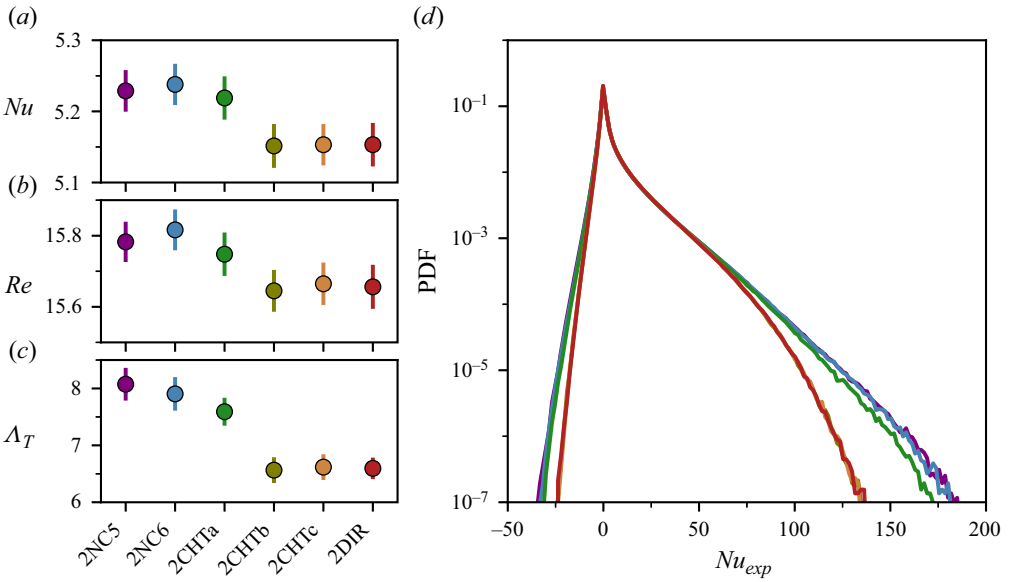

Figure 3. *Effect of different (partly non-ideal) thermal boundary conditions. While the global (a,b) heat and momentum transport depend only weakly on the configuration at* $Ra = 2 \times 10^5$*, (c) the size of the large-scale flow structures is strongly influenced. Error bars depict the standard deviation; see table 2. In contrast to its global measure, (d) the statistical distribution of the local heat transport depends sensitively on the thermal boundary conditions.*

Figure 3 visualises the trends in the other three quantities with the applied thermal boundary conditions in panels (*a–c*). We find that both the global heat and momentum transport are enhanced by approximately 1 % when the configuration comprises a glass top plate. The origin of this intensification can be found in the enhanced buoyancy $\boldsymbol{b} = T\boldsymbol{e}_z$, the latter of which becomes possible due to the looser bound on the temperature field (here with $T < 0$ possible) when thermal inhomogeneities become significant at the boundaries. However, their impact on *Nu* and *Re* is tiny compared with an average 19 % increase in the size of long-living large-scale flow structures as measured by Λ_T. This underlines the effect of thermal boundary conditions or inhomogeneities at the boundaries on pattern formation.

Unfortunately, the experimentally present measurement techniques did not admit to determine $\partial T/\partial z$ as part of *Nu*. We thus extend our analysis of the (local) heat transfer to

$$Nu_{exp}(x, y, z = 0.5, t) := \sqrt{Ra\,Pr}\,u_z\Theta \quad \text{with } \Theta := T - T_{lin}, \tag{3.5}$$

where Θ represents the temperature deviation field around the linear conduction profile $T_{lin} := \langle T_b - (T_b - T_t)z\rangle_A \simeq 1 - z$. This experimentally accessible Nusselt number is one subset of the (true) Nusselt number introduced in (3.2), and its mean value can (provided $\langle \partial T/\partial z(z = 0.5)\rangle_A = 0$ and certain further criteria) coincide with that of *Nu* as described in more detail by Käufer *et al.* (2023).

We contrast the time-averaged probability density functions (PDFs) of Nu_{exp} in figure 3(*d*) for the entire set of considered domain configurations. Note that $Nu_{exp} > 0$ corresponds to regions of intended heat transfer with either $u_z > 0$ and $\Theta > 0$ or $u_z < 0$ and $\Theta < 0$, whereas $Nu_{exp} < 0$ corresponds to regions of inverted heat transfer with either $u_z > 0$ and $\Theta < 0$ or $u_z < 0$ and $\Theta > 0$. In contrast to the global values of *Nu* (see again panel *a*), we find that the statistical distribution of the (local) heat transfer depends sensitively on the thermal boundary conditions. The tails, especially the positive ones that comprise the very cold downwelling fluid, are significantly enhanced when thermal inhomogeneities are allowed at the boundaries. The PDF becomes thus wider as bounds on T get looser.

https://doi.org/10.1017/flo.2024.35 Published online by Cambridge University Press

We conclude this section by comparing our numerical configurations with data from the experiment, the latter of which we therefore include in tables 1 and 2. We find that both Nu_{exp} and Re are smaller or seem to be underestimated in the laboratory experiment. In contrast, Λ_T agrees well once a glass top plate is considered in the simulations. In other words, the numerical inclusion of solid plates with realistic thermophysical and geometrical properties allows us to explain the increased size of the flow pattern in the experiment. As the digital twin agrees best with the experiment when $Bi = 6.0$, we focus on this parameter in the following.

4. The impact of the experimental measurement procedure

As our digital twin with $Bi = 6.0$ successfully explains the increased flow pattern size from the experiment at $Ra = 2 \times 10^5$, we extend it towards the larger experimentally provided $Ra = \{4, 7\} \times 10^5$ (Moller 2022; Moller *et al.* 2022) and include the corresponding data in tables 1 and 2.

A comparison of the resulting size of large-scale flow structures confirms a good agreement between the numerical and experimental flows across the entire range of Rayleigh numbers, especially when keeping the standard deviation and limited field of view for the experimental data in mind. However, we find that the overall heat and momentum transfer persist to disagree strongly between both approaches. Both Nu_{exp} and Re seem to be underestimated by roughly 20 % in the experiment. Hence, we proceed by implementing and analysing the detailed effects of the experimentally present measurement procedure.

4.1. Numerical implementation of measurement errors and uncertainties

We emulate the effects of experiment measurements by considering the following aspects.

(1) The neglect of the vertical temperature gradient (i.e. affecting Nu or Nu_{exp}).
(2) Any spatial averaging (affecting u_z and T), both
    (a) vertically across a slab due to the light sheet thickness and
    (b) horizontally in interrogation windows as required for particle image velocimetry and thermometry (PIV and PIT, respectively).
(3) Thermal measurement deviations (only affecting T) associated with
    (a) an erroneous determination of plate temperatures from only a few point measurements and
    (b) uncertainties from the colour identification of thermochromic liquid crystals (TLCs).

For the flows at hand, the systematic omissions of (1) and (2a) affect Nu by only about 1 % and are thus considered to be negligible. As this agrees with Käufer *et al.* (2023), we disregard these two effects and focus on the effect of the remaining three aspects on Nu_{exp} in the following.

We apply a horizontal averaging in interrogation windows of an approximate size of (depending on Ra) 0.11^2 or 0.17^2 (Moller 2022; Moller *et al.* 2022) in dimensionless spatial coordinates to both $\boldsymbol{u}$ and T – this blurs those fields essentially. Furthermore, we manipulate the temperature field to incorporate the outlined systematic errors as well as random uncertainties. This is realised as follows.

Let

$$\tilde{T}^m = \frac{T^m - \langle T_t^m \rangle_{A,t}}{\Delta T^m} \quad \text{with } \Delta T^m = \langle T_b^m - T_t^m \rangle_{A,t} \tag{4.1}$$

be the resulting or perceived non-dimensional temperature for some measured (i.e. dimensional) local temperature value T^m. Any of the involved measured temperatures $\{T^m, T_b^m, T_t^m\}$ can be subject to individual errors and uncertainties via

$$T_{\Phi}^m = T_{\Phi} + \delta T_{\Phi}, \tag{4.2}$$

https://doi.org/10.1017/flo.2024.35 Published online by Cambridge University Press

with T_{Φ} representing the true value and δT_{Φ} the measurement deviation. This allows us to conclude that the perceived non-dimensional temperature is related via

$$\tilde{T}^m = \frac{\tilde{T} + \delta\tilde{T} - \langle \delta\tilde{T}_t \rangle_{A,t}}{\langle 1 + \delta\tilde{T}_b - \delta\tilde{T}_t \rangle_{A,t}} \equiv \underbrace{\frac{\tilde{T} - \langle \delta\tilde{T}_t \rangle_{A,t}}{\Delta\tilde{T}^m}}_{\substack{\textit{error solely due to} \\ \textit{plate temperatures}}} + \underbrace{\frac{\delta\tilde{T}}{\Delta\tilde{T}^m}}_{\substack{\textit{uncertainty} \\ \textit{due to TLCs}}} \qquad \text{with } \Delta\tilde{T}^m = \langle 1 + \delta\tilde{T}_b - \delta\tilde{T}_t \rangle_{A,t} \tag{4.3}$$

to the corresponding non-dimensional measurement deviation $\delta\tilde{T}_{\Phi} := \delta T_{\Phi}/\Delta T$, the latter of which are defined based on the true temperature difference across the fluid layer ΔT. In other words, we derived a framework to add non-dimensional measurement deviations $\delta\tilde{T}_{\Phi}$ to true non-dimensional values $\tilde{T}$. Note that $\delta\tilde{T}_{\Phi} > 0$ implies that the perceived value is larger than the true value; see (4.2).

Our approach allows us to disentangle the thermal measurement deviations $\{\delta\tilde{T}, \delta\tilde{T}_b, \delta\tilde{T}_t\}$ depending on their origin as shown on the right of (4.3). The amplitude of the TLC-related δT has been quantified in Moller (2022) as a function of the true temperature, i.e. we are given $\delta T = \delta T(T)$. We can make use of this relation in (4.3) via $\delta T/\Delta T^m \equiv \delta\tilde{T}/\Delta\tilde{T}^m$ – the associated standard deviation is on average 6 % of the perceived temperature drop across the fluid layer, but (depending on T and Ra) the local value can easily exceed 10 %. We model this random local uncertainty numerically as Gaussian noise. In contrast, the experimental data does not allow for an estimation of any systematic errors associated with the determination of the plate temperatures, $\langle \delta\tilde{T}_b \rangle_{A,t}$ and $\langle \delta\tilde{T}_t \rangle_{A,t}$.

We therefore estimate the latter based on a numerical imitation of the experimental plate temperature measurement. In the experiment (Moller 2022), $\langle T_b \rangle_A$ is determined based on five temperature probes within the bottom solid plate, whereas $\langle T_t \rangle_A$ is determined based on four sensors that are glued onto the top plate. Resembling this process with our digital twin, we find that this technique allows for capturing the bottom plate's mean temperature almost perfectly due to its homogeneous temperature distribution – the error is of the order of $O(10^{-4})$. This changes once the top plate with its thermal inhomogeneities is considered. Figure 4 tracks therefore the evolution of the temperature signals at the upper solid–fluid interface. Although $\langle T_t \rangle_A = 0$ already shortly after the initialisation, the local temperature signals fluctuate strongly. An arithmetic average dampens these fluctuations only to a certain extent. Crucially, even a time average of the instantaneous ensemble average does not yield the correct mean interface temperature – instead, we find deviations of approximately 5 % that are roughly similar to $\langle \mathrm{std}(T_t) \rangle_{A,t}$. Moreover, we find that the standard deviations agree with those of the experimentally obtained time series (Moller 2022). This analysis highlights that the temperature at the thermally inhomogeneous top plate varies strongly over space and time, and so four sensors are too few to identify the mean temperature at this solid–fluid interface accurately. The derived non-dimensional temperatures in the experiment might thus be biased. In the following, we drop the tildes and assume that $\langle \delta T_b \rangle_{A,t} = 0$ and $\langle \delta T_t \rangle_{A,t} = \langle \mathrm{std}(T_t) \rangle_{A,t}$.

4.2. The impact of measurement deviations on the (local) heat transfer

So far, we have described the origin of different experimentally present measurement errors and uncertainties, quantified their individual size and derived a framework to correspondingly modify numerical data. We proceed by adding key measurement effects to the numerical data at $Ra = 2 \times 10^5$ and analysing their effect on both the statistical and mean heat transfer in more detail.

Figure 5 visualises this iterative process, the latter of which starts with the ground truth of Nu_{exp} as defined in (3.5). Note that this ground truth is based on the unmodified numerical fields and already known from figure 3(*d*). In analogy to the PIV and PIT processing, we start by incorporating a horizontal averaging in interrogation windows. Since any spatial averaging dampens local extrema, the PDF's tails become weaker and it narrows significantly. Importantly, also the associated average decreases by 9 %. Next, we start perceiving the mean temperature of the upper solid–fluid interface hotter than it actually is. This leads to cold temperatures appearing even colder and so the range of observed temperature

https://doi.org/10.1017/flo.2024.35 Published online by Cambridge University Press

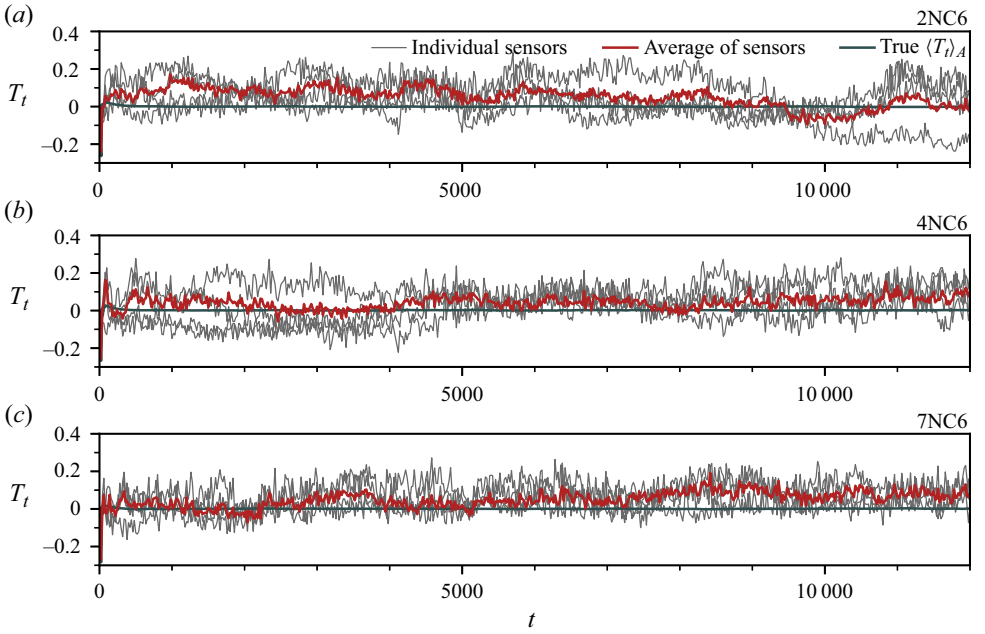

Figure 4. *Numerical top (glass) plate temperature measurement. Although the true mean interface temperature* $\langle T_t \rangle_A = 0$ *already after* $O(10^2 \tau_f)$*, four point sensors are too few to identify it accurately.*

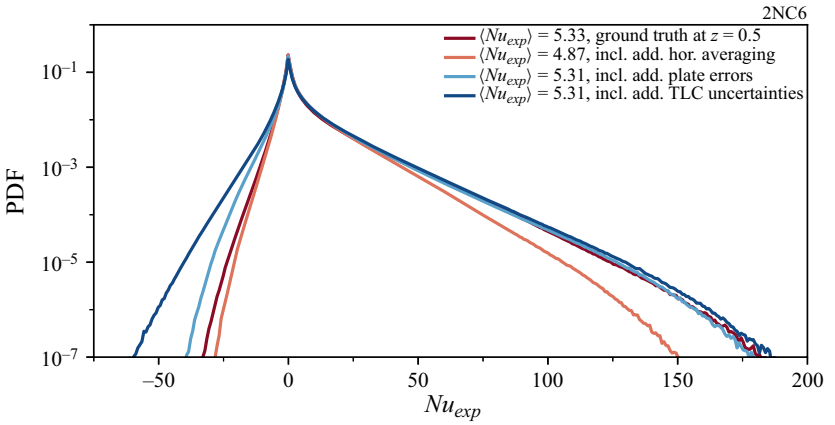

Figure 5. *Impact of the measurement procedure. Although the latter affects the perceived statistical distribution of the local heat transfer significantly, its mean value* $\langle Nu_{exp} \rangle$ *seems almost unchanged. Note that the different contributions outlined in the legend are applied cumulatively.*

values broadens. As a consequence, the PDF tails become stronger and the associated average increases by about 9 %. Including eventually also the TLC-related uncertainties spread the tails of the PDF beyond any of the previously plotted ones. This affects the weaker negative tails more strongly than the stronger positive ones due to the intricate composition of Nu_{exp}; see again § 3.3. Interestingly, the mean perceived heat transfer across the fluid layer is not affected despite the complex relation between δT and T.

After considering all these different aspects, $\langle Nu_{exp} \rangle$ is reduced by less than 1 % compared with its original value. However, the statistical heat transfer has been affected strongly in a way that depends sensitively on all of them.

https://doi.org/10.1017/flo.2024.35 Published online by Cambridge University Press

4.3. Comparison of laboratory measurements with manipulated numerical data

The previous §§ 3.3 and 4.2 have laid out the foundations to understand the detailed effects of experimentally present non-ideal thermal boundary conditions and uncertainties introduced by the measurement techniques, respectively. In this section we consider perceived, i.e. manipulated, numerical quantities only and so we omit any related superscript.

Figure 6(*a*) presents the resulting instantaneous temperature field $T(x, y, z = 0.5, t = t_r)$ from the numerical simulation at $Ra = 2 \times 10^5$ that mimics the experimental measurement procedure. A comparison with figure 2(*c*) highlights the impact of the latter. The perceived temperature fields at larger Rayleigh numbers are included in figure 6(*b*,*c*). Although the enhanced turbulence results in an increased mixing of the scalar temperature, the decreasing ratio of the pattern size to the horizontal extent of the domain, i.e. Λ_T/Γ, leads to a stronger influence of side walls on pattern formation – the long-living large-scale flow structures thus tend to align with the side walls.

Figure 6(*d–f*) contrasts the perceived temperature distributions from the numerical simulations and laboratory experiments by means of their time-averaged PDFs. Note that we observe temperatures beyond the range $[0, 1]$ due to two independent reasons. Firstly, the non-ideal thermal boundary conditions allow for spatial variations of the temperature field at the solid–fluid interfaces. With $\kappa_{sb}/\kappa_{fl} \sim O(10^2) \gg \kappa_{st}/\kappa_{fl} \sim O(10^0)$, this affects practically solely the lower limit of T (see again § 3.3). Secondly, the uncertainties associated with the TLC measurements cause the detection of temperatures beyond both sides of $[0, 1]$. Any ramification on either of these bounds depends on the functional dependence $\delta T = \delta T(T)$. As a result, we detect in both the modified numerical as well as the experimental data temperatures beyond the spatio-temporal averages $\langle T_t \rangle_{A,t} = 0$ and $\langle T_b \rangle_{A,t} = 1$.

The perceived numerical data shows slightly stronger tails for lower temperatures compared with the higher ones. We find that these left tails, as well as the peaks, coincide very well with the experimental data; see, in particular, panel (*f*). However, the laboratory measurements show an over-representation of larger temperatures, especially at larger *Ra*. This is related to locally increased uncertainties of the TLCs at higher temperatures and observation angles (König *et al.* 2019; Moller *et al.* 2019, 2021; Moller 2022). For this reason, previous studies have disregarded any temperature measurements outside the range $[0, 1]$ (indicated by the grey shaded areas in figure 6*d–f*) (Moller 2022). If the situation was symmetric, this could be considered reasonable. However, as this ignores the natural asymmetry due to the thermal boundary conditions and TLC uncertainties, and to avoid sharp cutoffs at or due to large temperatures, we retain these measurements in this study.

Figure 6(*g–i*) opposes the perceived velocity components with respect to their time-averaged PDFs. An almost perfect match of the horizontal velocities $u_{x,y}$ between the numerical and experimental approach confirms the good resemblance of the latter by its digital twin. The buoyancy-driven convective heat transport induces vertical velocities that exceed the horizontal ones. Although this is true for both data sources, vertical velocities from the simulations are significantly stronger compared with those from the experiments. Since this cannot be resolved by our digital twin and the applied modifications, it suggests that the vertical or out-of-plane component of the velocity might have been systematically (i.e. independently of *Ra*) underestimated by the stereoscopic PIV measurements.

Building up on the above insights, figure 6(*j–l*) compares the resulting experimentally accessible Nusselt number Nu_{exp}. On the one hand, we find that the PDFs offer a similar shape in panel (*j*) with a growing discrepancy towards larger *Ra*. This latter circumstance suggests that the over-representation of those tails can be attributed to the *Ra*-dependent increase of uncertainties associated with the TLC measurements; see again panels (*d–f*). On the other hand, we find that $\langle Nu_{exp} \rangle_{A,t} = \{5.31, 6.18, 7.56\}$ based on the manipulated numerical data. Since these values are, independently of *Ra*, larger than the experimentally observed ones (see again table 2), this supports the suspicion of an experimental underestimation of the vertical velocity (see again panels *g–i*).

https://doi.org/10.1017/flo.2024.35 Published online by Cambridge University Press

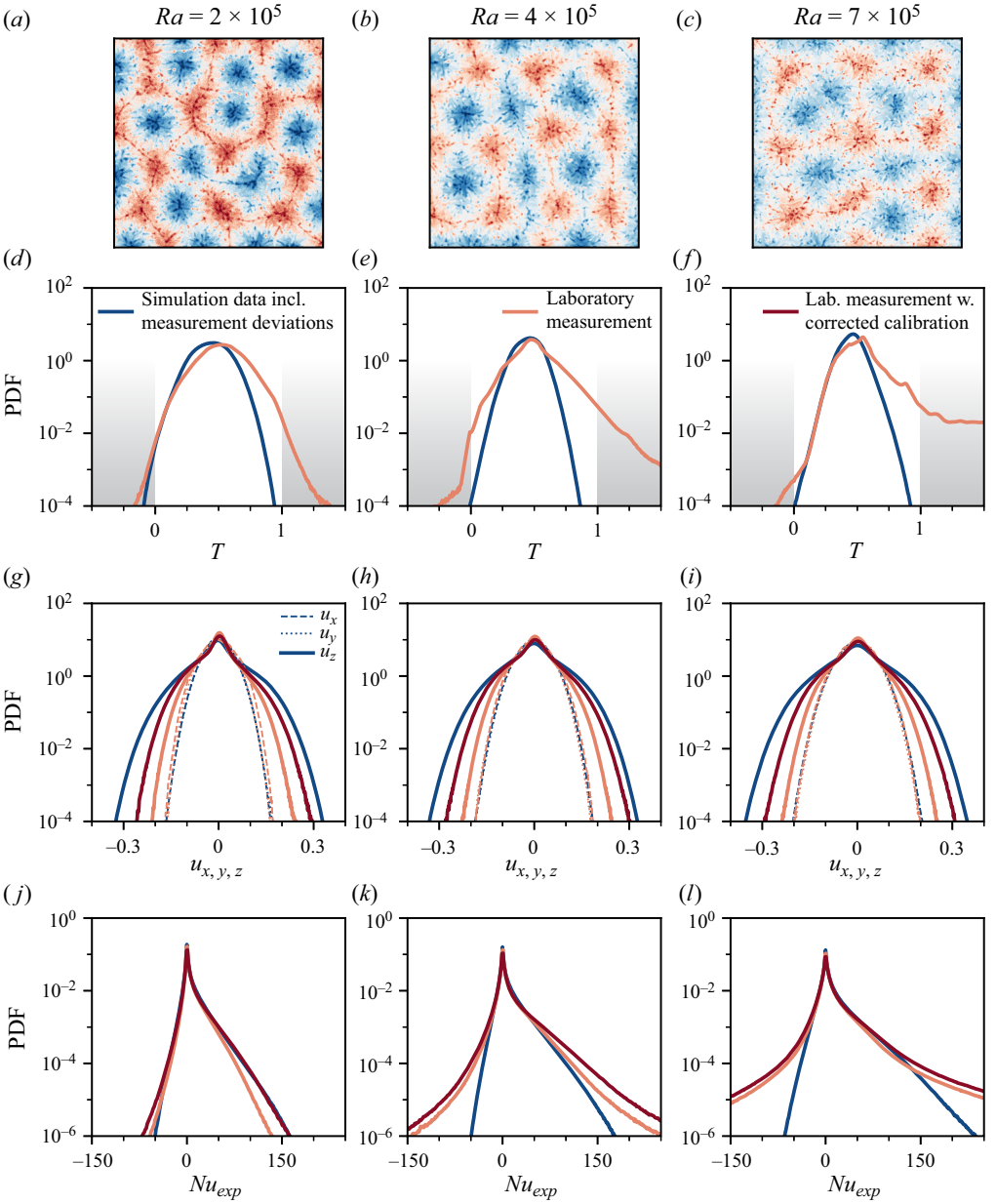

Figure 6. *Contrast of statistical data obtained from simulations and experiments. Here we exploit simulation data at Bi = 6.0 only – see panels (a–c) for instantaneous temperature fields $T(x, y, z = 0.5, t = t_r)$ that are subjected to experiment-like measurement deviations. The colour map coincides with figure 2 and the corresponding Ra are given at the top. Below, the statistical distribution of the (d–f) temperature T, (g–i) velocities $u_{x,y,z}$ and (j–l) experimentally accessible Nusselt number Nu_{exp} are contrasted with laboratory experimental data. Although the PDFs$(T, u_{x,y})$ seem to agree well between simulations and experiments, u_z appears to be underestimated in the case of the latter across all Ra. The correction of the subsequently discovered calibration mistake allows for an improved convergence of results. The second row defines the colour encoding for all the PDFs, whereas its grey backgrounds indicate measurements that used to be discarded in past experiments.*

https://doi.org/10.1017/flo.2024.35 Published online by Cambridge University Press

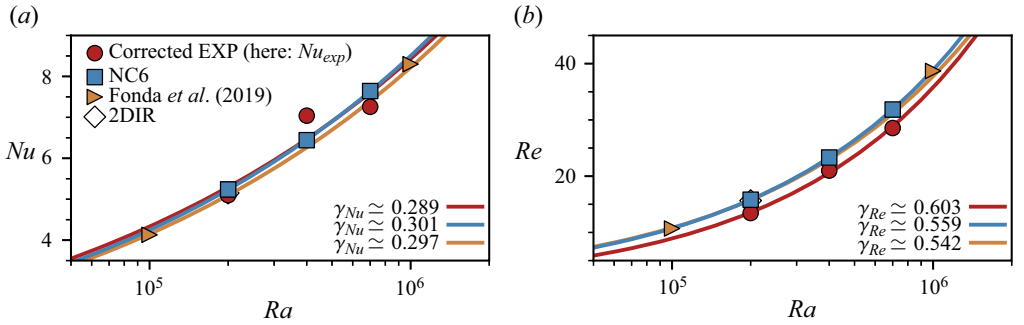

Figure 7. *Scaling of the global heat and momentum transfer. We contrast available experimental and numerical data – that offer both $Pr \simeq 7$ and a closed Cartesian domain with $\Gamma = 25$ – between (i) idealised constant temperature and (ii) experiment-like conditions. Markers specify the exact data points whereas solid lines represent the resulting (extrapolated) fitted curves with the corresponding scaling exponents provided in the legends. Fonda et al. (2019) offers numerical data at constant temperature conditions.*

4.4. Reassessment of the original laboratory measurement data

Even after resembling the laboratory measurement procedure, our digital twins offer an increased global heat transfer compared with the experiment. As our data suggests an experimental underestimation of u_z, $\langle Nu_{exp} \rangle_{A,t} \sim u_z$ appears to be roughly 22 % larger in the case of the former compared with the latter.

We therefore carefully scrutinise or reassess the processing of the original stereo-PIV measurement data starting from the raw uncalibrated camera images. This reveals that the previously used pinhole camera calibration model with a subsequent self-calibration (Wieneke 2005) did not account for the optical refraction effect between the cameras and the fluid layer, resulting in wrong vertical distances of the calibration planes and, thus, a systematic underestimation of only the vertical or out-of-plane velocity component. This issue can be eliminated by using a polynomial calibration that creates the image-to-world mapping by fitting polynomials through the calibration markers. This approach does not require any modelling of the optical path and is well suited for complex set-ups. As a downside, it allows for limited extrapolations beyond the calibrated region only; this is not of relevance for us anyway. We thus reprocess the PIV data using a polynomial calibration and find a relative increase of u_z by approximately 24 % for all different Rayleigh numbers. As this number propagates directly to Nu_{exp}, they agree now almost perfectly with the expectations based on the digital twin. This reassessment reveals new (corrected) global measures of heat and momentum transport in the laboratory experiment of $Nu_{exp} = \{5.09, 7.04, 7.25\}$ and $Re = \{13.56, 20.99, 28.55\}$, respectively. Figure 6(*g–l*) also includes the corrected statistical data.

Finally, it is certainly of interest how these corrected values and the thermal boundary conditions more generally affect the overall scaling of the global heat and momentum transfer. We thus conclude with a detailed comparison of Nu and Re in figure 7. First, we find that the corrected data points from the experiment offer an improved conformity with its digital twin NC6. While Nu_{exp} at $Ra = 4 \times 10^5$ seems to stand out in this direct comparison, we can trace this back to the usage of a different temperature calibration for this single experiment run. Nevertheless, we find that the resulting scaling exponents describing $Nu \sim Ra^{\gamma_{Nu}}$ (Plumley & Julien 2019; Vieweg 2023) and $Re \sim Ra^{\gamma_{Re}}$ are quite similar. This confirms that the underlying physics of the flow is properly captured by the experimental measurement data and that this physics's detection is mostly unaffected by the measurement deviations. Second, contrasting the digital twin NC6 with numerical data at constant temperature boundary conditions from Fonda *et al.* (2019) and our simulation 2DIR underlines the marginal effect of variations of thermal boundary conditions (as far as considered in this study) on both quantities. We find the scaling exponents to coincide virtually and the resulting fitted curves to be almost congruent. This comparison confirms our results from § 3.3 at $Ra = 2 \times 10^5$ and extends them across the range $Ra = [2, 7] \times 10^5$.

https://doi.org/10.1017/flo.2024.35 Published online by Cambridge University Press

5. Discussion and perspective

This comparative study has systematically scrutinised discrepancies between observations from numerical and experimental approaches. In particular, the long-living large-scale flow structures (Käufer *et al.* 2023; Vieweg 2023, 2024) seemed to show an increased characteristic size but decreased induced heat transfer in an experimental approach relative to numerical ones. As constraints emerging from the measurement techniques limit corresponding modifications to the experiment set-up, we decided to shift perspectives and use simulations instead.

Both the horizontal extent of the domain as well as the interaction of the fluid layer with the adjacent solid plates are of crucial significance for the formation of flow structures and, thus, their induced heat transfer (Krug *et al.* 2020; Vieweg *et al.* 2021*b*). Past numerical studies have not accounted for these two aspects simultaneously (Czarnota & Wagner 2013; Pandey *et al.* 2018; Foroozani *et al.* 2021; Vieweg *et al.* 2021*b*; Käufer *et al.* 2023). Hence, we created a digital twin of the laboratory experiment by including the solid plates with respect to their geometry, thermophysical properties and respective external thermal boundary conditions.

We find that, for this twin, $\max(\Delta_{hor}T_t) > 0.5$ and, thus, exceeds half of the total temperature drop ΔT across the fluid layer for all Ra. This shows that the upper solid–fluid interface is extremely prone to thermal inhomogeneities and proves that the past assumption 'the isothermal boundary conditions can be considered as fulfilled in good approximation' (Moller *et al.* 2020) has to be reconsidered for the experimentally covered range of Ra. Only the bottom aluminium plate renders the corresponding interface isothermal. A comparison of the different convection and heat transfer coefficients $\{h_{Bi}, h_{st}, h_{fl}, h_{sb}\}$ across the different layers (see again (2.15*d*) and (2.15*e*)) shows that thermal conduction across the top plate represents the essential bottleneck for heat transfer in the domain and, thus, alters the boundary conditions significantly. For instance, $h_{st}/h_{fl} \approx 1.6$ in contrast to $h_{Bi}/h_{fl} \approx 2.9$ and $h_{sb}/h_{fl} \approx 126$ for $Ra = 2 \times 10^5$. As is underlined by simulation 2CHTa (corresponding to $h_{Bi} \rightarrow \infty$), the effect of increasing Bi is very limited.

A systematic stepwise simplification of the digital twin to the standard numerical set-up shows that realistic thermophysical properties do explain the experimentally observed increased structure size Λ_T – confirming our previous results (Vieweg *et al.* 2021*b*; Vieweg 2023) – but not the decreased Nu_{exp}. Questioning the experimentally present measurement procedure, we continued by resembling it in a controlled manner based on the exact high-resolution data from its digital twin and, thus, extended our previous work (Käufer *et al.* 2023) to examine the sensitivity to different experimental uncertainties. Although we find that (i) four temperature probes are too few to correctly identify the mean upper solid–fluid interface temperature, and (ii) the statistical heat transfer is clearly affected by the measurement procedure – indicating a contradiction to our conclusion drawn in Käufer *et al.* (2023) – there is practically no impact of this procedure on the average heat transfer.

Eventually, the comparison of the vertical velocities u_z from both the experiment and its digital twin suggested a systematic underestimation in the case of the former. In fact, this out-of-plane velocity component is most susceptible to systematic measurement errors during stereoscopic PIV (Westerweel 1997; Prasad 2000; Cierpka *et al.* 2012; Raffel *et al.* 2018) with an exact calibration being key (Prasad 2000; Wieneke 2005). A subsequent reassessment of the original stereo-PIV measurement data starting from the raw camera images revealed indeed a camera calibration error in Moller *et al.* (2021, 2022) and Moller (2022) and, thus, also the data used in Käufer *et al.* (2023) and Teutsch *et al.* (2023), underestimating the distances between the calibration planes. Correcting this mistake results in a 24 % relative increase of u_z – the latter's sign and distribution, as well as the size and temporal evolution of flow structures, are not affected. This allows us to finally collapse the data from both the laboratory experiment as well as the numerical simulations across the entire range of considered Ra, particularly with respect to Nu. This resolves the remaining motivating discrepancies.

This study highlights that digital twins represent, together with the resemblance of laboratory measurement procedures, a highly useful tool for resolving discrepancies between experimental and

https://doi.org/10.1017/flo.2024.35 Published online by Cambridge University Press

numerical observations and, thus, drive the progress in thermofluid science with its numerous applications. From an experimental perspective, our study suggests moving towards volumetric Lagrangian particle tracking techniques to prevent incorrect reconstructions of individual velocity components (Käufer & Cierpka 2024). Especially in combination with physics-informed machine learning, this allows for revealing even more information of the flow (Toscano *et al.* 2024). From a physical perspective, our study underlines the crucial role of realistic thermal boundary conditions with respect to the formation of long-living large-scale flow structures as well as their characteristic size and lifetime. It is clear that this point becomes even more important when the geometry of the heat transfer system goes beyond a simple cuboid configuration as discussed here. Understanding the effect of symmetric non-ideal thermal boundary conditions is essential for a successful interpretation of more complex configurations and will be addressed in a future study. Another point that has to be left open for future work is the impact of these non-ideal boundary effects at higher Rayleigh numbers.

Acknowledgments. The authors are very grateful to Bernd Wieneke and Dirk Michaelis from LaVison GmbH for discussing the impact of the different camera calibration models.

Funding statement. P.P.V. is funded by the Deutsche Forschungsgemeinschaft (DFG, German Research Foundation) within Walter Benjamin Programme 532721742. T.K. and C.C. are supported by the Carl Zeiss Foundation within project number P2018-02-001 'Deep Turb – Deep Learning in and of Turbulence' and by the DFG within project number 467227170. P.P.V. gratefully acknowledges the computing centre of the Technische Universität Ilmenau for providing access to, as well as computing and storage resources on its compute cluster MaPaCC24.

Declaration of interests. The authors report no conflict of interest.

Data availability statement. Supporting data to this study can be made available by the authors upon reasonable request.

Author contributions. P.P.V. designed the study, prepared and performed the numerical simulations, plotted the figures and drafted the manuscript. T.K. provided the experiment data based on (Moller *et al.* 2021; Moller 2022) and reprocessed it with C.C.. All authors contributed equally in discussing the data and finalising the paper.

References

Atkinson, B.W. & Wu Zhang, J. 1996 Mesoscale shallow convection in the atmosphere. *Rev. Geophys*. **34**, 403–431.

Bénard, H. 1901 Les tourbillons cellulaires dans une nappe liquide transportant de la chaleur par convection en régime permanent. *Ann. Chim. Phys*. **23**, 62–144.

Bhattacharya, S. & Vlachos, P.P. 2020 Volumetric particle tracking velocimetry (PTV) uncertainty quantification. *Exp. Fluids* **61**, 197.

Boeck, T. 2000 Bénard–Marangoni convection at low Prandtl numbers: results of direct numerical simulations. In *Berichte aus der Physik*. Shaker.

Boussinesq, J.V. 1903 *Théorie Analytique de La Chaleur*, vol. 2. Gauthier-Villars.

Bown, M.R., MacInnes, J.M., Allen, R.W.K. & Zimmerman, W.B.J. 2006 Three-dimensional, three-component velocity measurements using stereoscopic micro-PIV and PTV. *Meas. Sci. Technol*. **17**, 2175–2185.

Chapman, C.J., Childress, S. & Proctor, M.R.E. 1980 Long wavelength thermal convection between non-conducting boundaries. *Earth Planet. Sci. Lett*. **51**, 362–369.

Chapman, C.J. & Proctor, M.R.E. 1980 Nonlinear Rayleigh–Bénard convection between poorly conducting boundaries. *J. Fluid Mech*. **101**, 759–782.

Cierpka, C., Rossi, M., Segura, R., Mastrangelo, F. & Kähler, C.J. 2012 A comparative analysis of the uncertainty of astigmatism-μPTV, stereo-μPIV, and μPIV. *Exp. Fluids* **52**, 605–615.

Czarnota, T. & Wagner, C. 2013 Turbulent convection in a Rayleigh–Bénard cell with solid horizontal plates of finite conductivity. In *New Results in Numerical and Experimental Fluid Mechanics VIII* (ed. A. Dillmann, G. Heller, H.P. Kreplin, W. Nitsche & I. Peltzer), pp. 607–614. Springer.

Fischer, P.F. 1997 An overlapping Schwarz method for spectral element solution of the incompressible Navier–Stokes equations. *J. Comput. Phys*. **133**, 84–101.

Fonda, E., Pandey, A., and Schumacher, J. & Sreenivasan, K.R. 2019 Deep learning in turbulent convection networks. *Proc. Natl Acad. Sci. USA* **116**, 8667–8672.

Foroozani, N., Krasnov, D. & Schumacher, J. 2021 Turbulent convection for different thermal boundary conditions at the plates. *J. Fluid Mech*. **907**, A27.

Hashim, I. & Wilson, S.K. 1999 The onset of Bénard–Marangoni convection in a horizontal layer of fluid. *Intl J. Engng Sci*. **37**, 643–662.

Hau, E. 2013 *Wind Turbines: Fundamentals, Technologies, Application, Economics*. Springer.

https://doi.org/10.1017/flo.2024.35 Published online by Cambridge University Press

Hurle, D.T.J., Jakeman, R. & Pike, E.R. 1967 On the solution of the Bénard problem with boundaries of finite conductivity. *Proc. R. Soc. Lond.* A **296**, 469–475.

Incropera, F.P. & DeWitt, D.P. 1996 *Fundamentals of Heat and Mass Transfer*. Wiley & Sons.

Johnston, H. & Doering, C.R. 2009 Comparison of turbulent thermal convection between conditions of constant temperature and constant flux. *Phys. Rev. Lett.* **102**, 064501.

Käufer, T. & Cierpka, C. 2024 Volumetric Lagrangian temperature and velocity measurements with thermochromic liquid crystals. *Meas. Sci. Technol.* **35**, 035301.

Käufer, T., Vieweg, P.P., Schumacher, J. & Cierpka, C. 2023 Thermal boundary condition studies in large aspect ratio Rayleigh–Bénard convection. *Eur. J. Mech.* B-*Fluids* **101**, 283–293.

König, J., Moller, S., Granzow, N. & Cierpka, C. 2019 On the application of a supercontinuum white light laser for simultaneous measurements of temperature and velocity fields using thermochromic liquid crystals. *Exp. Therm. Fluid Sci.* **109**, 109914.

Krug, D., Lohse, D. & Stevens, R.J.A.M. 2020 Coherence of temperature and velocity superstructures in turbulent Rayleigh–Bénard flow. *J. Fluid Mech.* **887**, A2.

Manneville, P. 2006 Rayleigh–Bénard convection: thirty years of experimental, theoretical, and modeling work. In *Dynamics of Spatio-Temporal Cellular Structures* (ed. I. Mutabazi, J.E. Wesfreid & E. Guyon), Springer Tracts in Modern Physics, vol. 207, pp. 41–65. Springer.

Moller, S. 2022 Experimental characterization of turbulent superstructures in large aspect ratio Rayleigh–Bénard convection. PhD thesis, TU Ilmenau.

Moller, S., Käufer, T., Pandey, A., Schumacher, J. & Cierpka, C. 2022 Combined particle image velocimetry and thermometry of turbulent superstructures in thermal convection. *J. Fluid Mech.* **945**, A22.

Moller, S., König, J., Resagk, C. & Cierpka, C. 2019 Influence of the illumination spectrum and observation angle on temperature measurements using thermochromic liquid crystals. *Meas. Sci. Technol.* **30**, 084006.

Moller, S., Resagk, C. & Cierpka, C. 2020 On the application of neural networks for temperature field measurements using thermochromic liquid crystals. *Exp. Fluids* **61**, 111.

Moller, S., Resagk, C. & Cierpka, C. 2021 Long-time experimental investigation of turbulent superstructures in Rayleigh–Bénard convection by noninvasive simultaneous measurements of temperature and velocity fields. *Exp. Fluids* **62**, 64.

Nobili, C. 2023 The role of boundary conditions in scaling laws for turbulent heat transport. *Math. Engng* **5**, 1–41.

Oberbeck, A. 1879 Ueber die wärmeleitung der flüssigkeiten bei berücksichtigung der strömungen infolge von temperaturdifferenzen. *Ann. Phys. Chem.* **243**, 271–292.

Otero, J., Wittenberg, R.W., Worthing, R.A. & Doering, C.R. 2002 Bounds on Rayleigh–Bénard convection with an imposed heat flux. *J. Fluid Mech.* **473**, 191–199.

Pandey, A., Scheel, J.D. & Schumacher, J. 2018 Turbulent superstructures in Rayleigh–Bénard convection. *Nat. Commun.* **9**, 2118.

Parodi, A., von Hardenberg, J., Passoni, G., Provenzale, A. & Spiegel, E.A. 2004 Clustering of plumes in turbulent convection. *Phys. Rev. Lett.* **92**, 194503.

Perelman, T.L. 1961 On conjugated problems of heat transfer. *Intl J. Heat Mass Transfer* **3**, 293–303.

Plumley, M. & Julien, K. 2019 Scaling laws in Rayleigh–Bénard convection. *Earth Space Sci.* **6**, 1580–1592.

Prasad, A.K. 2000 Stereoscopic particle image velocimetry. *Exp. Fluids* **29**, 103–116.

Pulkkinen, T. 2007 Space weather: terrestrial perspective. *Living Rev. Solar Phys.* **4**, 1.

Raffel, M., Willert, C.E., Scarano, F., Kähler, C.J., Wereley, S.T. & Kompenhans, J. 2018 *Particle Image Velocimetry: A Practical Guide*. Springer International Publishing.

Rayleigh, Lord 1916 On convection currents in a horizontal layer of fluid, when the higher temperature is on the under side. *Lond. Edinb. Dublin Phil. Mag. J. Sci.* **32**, 529–546.

Scheel, J.D., Emran, M.S. & Schumacher, J. 2013 Resolving the fine-scale structure in turbulent Rayleigh–Bénard convection. *New J. Phys.* **15**, 113063.

Scheel, J.D. & Schumacher, J. 2017 Predicting transition ranges to fully turbulent viscous boundary layers in low Prandtl number convection flows. *Phys. Rev. Fluids* **2**, 123501.

Schneide, C., Vieweg, P.P., Schumacher, J. & Padberg-Gehle, K. 2022 Evolutionary clustering of Lagrangian trajectories in turbulent Rayleigh–Bénard convection flows. *Chaos* **32**, 013123.

Schwenn, R. 2006 Space weather: the solar perspective. *Living Rev. Solar Phys.* **3**, 2.

Shabany, Y. 2010 *Heat Transfer: Thermal Management of Electronics*. CRC Press.

Stevens, R.J.A.M., Lohse, D. & Verzicco, R. 2014 Sidewall effects in Rayleigh–Bénard convection. *J. Fluid Mech.* **741**, 1–27.

Teutsch, P., Käufer, T., Mäder, P. & Cierpka, C. 2023 Data-driven estimation of scalar quantities from planar velocity measurements by deep learning applied to temperature in thermal convection. *Exp. Fluids* **64**, 191.

Toscano, J.D., Käufer, T., Maxey, M., Cierpka, C. & Karniadakis, G.E. 2024 Inferring turbulent velocity and temperature fields and their statistics from Lagrangian velocity measurements using physics-informed Kolmogorov–Arnold networks. arXiv:2407.15727.

Vallis, G.K. 2017 *Atmospheric and Oceanic Fluid Dynamics: Fundamentals and Large-Scale Circulation*. Cambridge University Press.

Vieweg, P.P. 2023 Large-scale flow structures in turbulent Rayleigh–Bénard convection: dynamical origin, formation, and role in material transport. PhD thesis, TU Ilmenau.

https://doi.org/10.1017/flo.2024.35 Published online by Cambridge University Press

Vieweg, P.P. 2024 Supergranule aggregation: a Prandtl number-independent feature of constant heat flux-driven convection flows. *J. Fluid Mech*. **980**, A46.

Vieweg, P.P., Klünker, A., Schumacher, J. & Padberg-Gehle, K. 2024 Lagrangian studies of coherent sets and heat transport in constant heat flux-driven turbulent Rayleigh–Bénard convection. *Eur. J. Mech.* B-*Fluids* **103**, 69–85.

Vieweg, P.P., Scheel, J.D. & Schumacher, J. 2021*b* Supergranule aggregation for constant heat flux-driven turbulent convection. *Phys. Rev. Res*. **3**, 013231.

Vieweg, P.P., Scheel, J.D., Stepanov, R. & Schumacher, J. 2022 Inverse cascades of kinetic energy and thermal variance in three-dimensional horizontally extended turbulent convection. *Phys. Rev. Res*. **4**, 043098.

Vieweg, P.P., Schneide, C., Padberg-Gehle, K. & Schumacher, J. 2021*a* Lagrangian heat transport in turbulent three-dimensional convection. *Phys. Rev. Fluids* **6**, L041501.

Westerweel, J. 1997 Fundamentals of digital particle image velocimetry. *Meas. Sci. Technol*. **8**, 1379–1392.

Wieneke, B. 2005 Stereo-PIV using self-calibration on particle images. *Exp. Fluids* **39**, 267–280.

Cite this article: Vieweg P.P., Käufer T., Cierpka C., Schumacher J. (2025). Digital twin of a large-aspect-ratio Rayleigh–Bénard experiment: role of thermal boundary conditions, measurement errors and uncertainties. *Flow*, *5*, E4. doi:10.1017/flo.2024.35